AGU PUBLICATIONS

JGR

Journal of Geophysical Research: Space Physics

RESEARCH ARTICLE
10.1002/2015JA022242

Key Points:
- A new method to reconstruct magnetosphere from data with no a priori assumptions about currents
- Faithfully reproduces magnetic effects of all major current systems and their changes during storms
- Can be used as a tool to reconstruct magnetospheric currents at a desired spatial resolution

Supporting Information:
- Supporting Information S1

Correspondence to:
N. A. Tsyganenko,
n.tsyganenko@spbu.ru

Citation:
Andreeva, V. A., and N. A. Tsyganenko (2016), Reconstructing the magnetosphere from data using radial basis functions, *J. Geophys. Res. Space Physics*, *121*, 2249–2263, doi:10.1002/2015JA022242.

Received 4 DEC 2015
Accepted 25 FEB 2016
Accepted article online 27 FEB 2016
Published online 18 MAR 2016

Reconstructing the magnetosphere from data using radial basis functions

Varvara A. Andreeva[1] and Nikolai A. Tsyganenko[1]

[1]Institute and Department of Physics, Saint Petersburg State University, Saint Petersburg, Russia

Abstract A new method is proposed to derive from data magnetospheric magnetic field configurations without any a priori assumptions on the geometry of electric currents. The approach utilizes large sets of archived satellite data and uses an advanced technique to represent the field as a sum of toroidal and poloidal parts, whose generating potentials Ψ_1 and Ψ_2 are expanded into series of radial basis functions (RBFs) with their nodes regularly distributed over the 3-D modeling domain. The method was tested by reconstructing the inner and high-latitude field within geocentric distances up to 12 R_E on the basis of magnetometer data of Geotail, Polar, Cluster, Time History of Events and Macroscale Interactions during Substorms, and Van Allen space probes, taken during 1995–2015. Four characteristic states of the magnetosphere before and during a disturbance have been modeled: a quiet prestorm period, storm deepening phase with progressively decreasing *SYM-H* index, the storm maximum around the negative peak of *SYM-H*, and the recovery phase. Fitting the RBF model to data faithfully resolved contributions to the total magnetic field from all principal sources, including the westward and eastward ring current, the tail current, diamagnetic currents associated with the polar cusps, and the large-scale effect of the field-aligned currents. For two main phase conditions, the model field exhibited a strong dawn-dusk asymmetry of the low-latitude magnetic depression, extending to low altitudes and partly spreading sunward from the terminator plane in the dusk sector. The RBF model was found to resolve even finer details, such as the bifurcation of the innermost tail current. The method can be further developed into a powerful tool for data-based studies of the magnetospheric currents.

1. Introduction

The inner and high-latitude magnetosphere is the most interesting, complex, and practically important region of the geospace, strongly affected by space weather events. Modeling its structure and dynamics is a challenging task extending beyond the scope of MHD simulations; for this reason the empirical modeling still remains an indispensable tool to describe and understand the near-Earth magnetic field.

At the beginning of the space era, the shortage of data was alleviated in first empirical models by qualitative a priori assumptions on the spatial configuration of the principal field sources. For example, in the T89 model [*Tsyganenko*, 1989] the symmetric ring current was represented by a single spread-out circular loop, whose radius and the total current were derived from observations. However, any prepostulated assertion about the field source geometry limits from the outset the model's ability to extract new information from the data. The first successful attempt to reduce the share of a priori assumptions in formulating a model was made by *Tsyganenko and Sitnov* [2007] (abbreviated henceforth as TS07), who represented the magnetic field of equatorial sources by extensible expansions into Fourier series and revealed peculiar features of the low-latitude currents during magnetospheric storms. At the same time, the equatorial current in that model was confined by construction inside a layer of prescribed thickness with a simple bell-shaped transverse profile of the current density, complemented by a custom-tailored system of field-aligned currents (FACs). In addition, the geodipole tilt-related deformation of the equatorial current was also rigidly prescribed from the outset.

In the last decade the amount of spacecraft data and the spatial density of data coverage enormously increased. In view of that, a natural question arises, whether it is possible to remove all a priori assumptions and to build a general model relying only on data and capable to reproduce the magnetospheric structure at a desired resolution. The goal of this work is to present a method to develop such a data-based model, free of any postulates on the electric current geometry, and to demonstrate its feasibility and performance. We generalize the TS07 approach to 3-D space by representing the model field as a formal sum of toroidal and poloidal

parts, whose generating functions are in turn expanded into linear combinations of radial basis functions (RBFs). The method is tested by reconstructing from data the magnetic field configurations, corresponding to four typical phases of a magnetospheric storm.

The paper consists of seven sections. Section 2 describes the method and is followed by section 3 outlining the data sets and their sources. Section 4 describes the model testing, and sections 5 and 6 present main results of the work and discuss them in terms of the underlying electric current systems. Section 7 summarizes the paper.

2. Method Description

The approach is based on representing the magnetic field **B** of extraterrestrial currents as the sum of toroidal and poloidal components [*Stern*, 1976; *Wolf-Gladrow*, 1987]:

$$\mathbf{B}(\mathbf{r}) = \nabla \times (\Psi_1 \mathbf{r}) + \nabla \times \nabla \times (\Psi_2 \mathbf{r}) = \nabla \Psi_1 \times \mathbf{r} + \nabla \times (\nabla \Psi_2 \times \mathbf{r}) \tag{1}$$

where $\Psi_1(\mathbf{r})$ and $\Psi_2(\mathbf{r})$ are the toroidal and poloidal generating functions and **r** is the radius vector. The choice of $\Psi_1(\mathbf{r})$ and $\Psi_2(\mathbf{r})$ is formally not restricted, and the field derived from (1) is always divergence free by construction. A standard way to create a flexible model, capable of describing a large variety of possible field configurations, is to expand Ψ_1 and Ψ_2 into linear combinations of some orthogonal basis functions. In its general features, such an approach was outlined in a review by *Stern* [1976]. *Kosik* [1989, 1998] developed a data-based model which included only the poloidal component, with the generating function Ψ_2 being limited to a sum of a few spherical harmonics.

In the present work, we explore a completely different way to represent the generating potentials: instead of using the orthogonal harmonics, we expand them into linear combinations of radial basis functions (henceforth RBFs) [e.g., *Buhmann*, 2003], that is, scalar functions χ_i depending only on the radial distance from the observation point **r** to a fixed center (or node) $\mathbf{R_i}$. The generating functions can then be represented as the linear expansions over a set of RBF centers distributed throughout the modeling domain:

$$\Psi_{1,2}(\mathbf{r}) = \sum_{i=1}^{N} a_{i_{1,2}} \chi_i(|\mathbf{r} - \mathbf{R_i}|) \tag{2}$$

A remarkable advantage of this approach is the possibility to locally adjust the density of RBF centers to improve the fit quality in specific regions [*Gershenfeld*, 2003]. After having tried several possible RBF forms, we chose the following one which provided the best results:

$$\chi_i = \sqrt{|\mathbf{r} - \mathbf{R_i}|^2 + D^2} \tag{3}$$

where D is an adjustable regularizing parameter on the order of a few distances between the neighboring nodes. To build an RBF-based model of the entire magnetosphere including the distant tail is hardly a manageable task, mostly because of too many RBF centers required to cover the vast region and related computational problems. Therefore, we focused on constructing such a model for the inner and high-latitude magnetosphere within $|\mathbf{r}| < 12\ R_E$. In the near-Earth region, the configuration of extraterrestrial field sources is mostly governed by the geodipole orientation rather than by the solar wind flow. For that reason, we formulate the model in the solar-magnetic (SM) coordinate system.

A fundamental property of the tilted magnetospheric configurations (following from that of the dipole field) is antisymmetry of B_x and B_y, and symmetry of B_z with respect to simultaneous change of sign of the z coordinate and of the dipole tilt angle ψ: $z \rightarrow -z$, $\psi \rightarrow -\psi$ [e.g., *Mead and Fairfield*, 1975, their equations (4)–(6)]

$$\begin{aligned} B_x(x, y, -z, -\psi) &= -B_x(x, y, z, \psi) \\ B_y(x, y, -z, -\psi) &= -B_y(x, y, z, \psi) \\ B_z(x, y, -z, -\psi) &= \ \ B_z(x, y, z, \psi) \end{aligned} \tag{4}$$

These relations reflect a general property of any magnetospheric configuration described in a dipole-centered coordinate system, which is the mutual mirror symmetry of any pair of configurations, corresponding to opposite values of the dipole tilt angle.

It can be easily verified that in order for the magnetic field (1) to satisfy the symmetry conditions (4), the toroidal and poloidal generating functions Ψ_1 and Ψ_2 must be even and odd, respectively, with regard to the above sign inversion. To construct the RBFs satisfying these requirements, we first combine the functions (3) in pairs, with their centers $\mathbf{R}_{i,+}$ and $\mathbf{R}_{i,-}$ located symmetrically on both sides of the SM equatorial plane. As a result, the RBFs $\chi_{i,e}$ and $\chi_{i,o}$ are obtained, which are even (hence the subscript "e") and odd ("o"), respectively, with regard to z:

$$\chi_{i,e}(\mathbf{r}) = \sqrt{|\mathbf{r}\text{-}\mathbf{R}_{i,+}|^2 + D^2} + \sqrt{|\mathbf{r}\text{-}\mathbf{R}_{i,-}|^2 + D^2} \equiv \chi_i^+ + \chi_i^- \tag{5}$$

$$\chi_{i,o}(\mathbf{r}) = \sqrt{|\mathbf{r}\text{-}\mathbf{R}_{i,+}|^2 + D^2} - \sqrt{|\mathbf{r}\text{-}\mathbf{R}_{i,-}|^2 + D^2} \equiv \chi_i^+ - \chi_i^- \tag{6}$$

where $\mathbf{R}_{i,+} = X_i\mathbf{e}_x + Y_i\mathbf{e}_y + Z_i\mathbf{e}_z$ and $\mathbf{R}_{i,-} = X_i\mathbf{e}_x + Y_i\mathbf{e}_y - Z_i\mathbf{e}_z$.

Then the generating functions $\Psi_1(\mathbf{r})$ and $\Psi_2(\mathbf{r})$ with the required type of symmetry can be written in the following form:

$$\Psi_1 = \cos\psi \sum_{i=1}^{N} a_i \left(\chi_i^+ + \chi_i^-\right) + \sin\psi \sum_{i=1}^{N} b_i \left(\chi_i^+ - \chi_i^-\right) \tag{7}$$

$$\Psi_2 = \cos\psi \sum_{i=1}^{N} c_i \left(\chi_i^+ - \chi_i^-\right) + \sin\psi \sum_{i=1}^{N} d_i \left(\chi_i^+ + \chi_i^-\right) \tag{8}$$

where a_i, b_i, c_i, and d_i are unknown coefficients representing contributions from the individual nodes and the summation is made over the entire 3-D set of N RBF centers. Note that in the most general case of arbitrary tilt angles, the $\cos\psi$ and $\sin\psi$ factors in (7) and (8) should be replaced by more general smooth functions having the same parities with respect to ψ. Due to relatively small values of $|\psi|$ in the case of terrestrial magnetosphere, we represent them by $\cos\psi$ and $\sin\psi$. As confirmed by test calculations described below, such an approximation remains quite accurate in the observed range of the tilt angles. Substituting (7) and (8) in (1) yields explicit equations for the field components. In order not to overload this section with lengthy algebra, their derivation is relegated to supporting information Text S1.

Several node placement schemes can in principle be implemented. In this work we constructed the RBF grid in spherical SM coordinates $\{r, \theta, \phi\}$ by distributing the nodes on a set of concentric spherical shells, centered at origin. In order to roughly equalize contributions of individual RBF nodes and, at the same time, keep their number at a reasonable minimum, the grid configuration is defined in such a way that the distance between the neighboring nodes lying on each shell is roughly uniform with respect to θ and ϕ. To build such a grid, a set of nearly equidistant nodes is first created on the innermost sphere with $R_1 = 2R_E$, using a placement method by *Kurihara* [1965], illustrated in Figure 1. Then the innermost spherical system of nodes is self-similarly replicated outward, such that the radial distance between the neighboring spheres gradually increases, to approximately match the growing lateral spacing between the nodes lying on the spheres of larger radius. In the present test version of the model the grid consisted of eight spherical layers, with the radii R_i of consecutive layers steadily increasing outward by a fixed factor, equal to $R_{i+1}/R_i = (N - 0.5 + \pi/4)/(N - 0.5 - \pi/4)$, where N is the prescribed number of latitude circles in the Northern Hemisphere (including the pole). In this model, we assumed $N = 7$, which produced a grid with the average distance between the nodes increasing from ~ 0.5 Re on the innermost layer with $R_1 = 2.0$ Re to $\sim 2\,R_E$ on the outermost sphere with $R_8 = 10.9\,R_E$.

Thus, generated grid contained in total 680 nodes in the northern hemispace, producing 680 RBFs $\chi_i^+(\mathbf{r}, \mathbf{R}_{i,+})$ and the same number of symmetric nodes in the southern hemispace with 680 conjugate functions $\chi_i^-(\mathbf{r}, \mathbf{R}_{i,-})$, entering in (7) and (8). The total number of the corresponding unknown coefficients a_i, b_i, c_i, and d_i would therefore be $680 \times 4 = 2720$. In such a formulation, however, the RBF model defined by equations (1) and (5)–(8) represents the magnetic field as only a function of the position vector $\mathbf{r}$ and the dipole tilt angle ψ. It yet remains to define input variables, quantifying the interplanetary impact on the magnetosphere and/or its current state. A parameter of primary importance here is the solar wind dynamic pressure, affecting all external field sources. Following the approach adopted in earlier models [*Sitnov et al.*, 2008; TS07], we directly

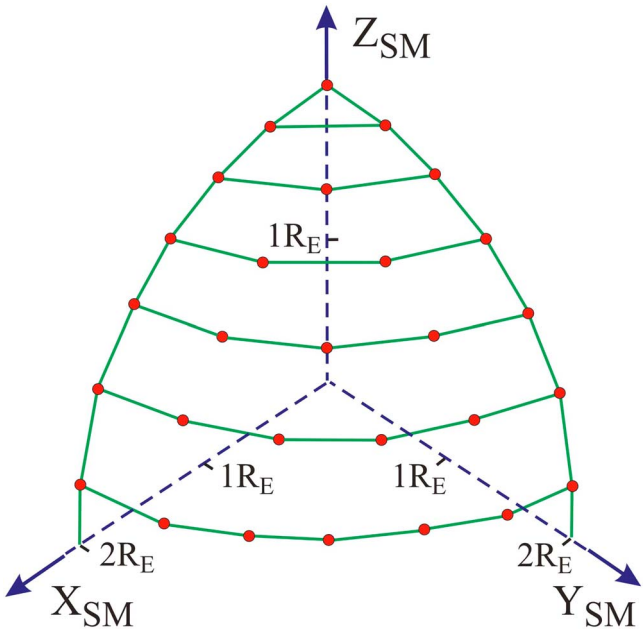

Figure 1. Illustrating the RBF node placement scheme according to *Kurihara*'s [1965] grid. Only the northern quarter of the innermost node layer is shown.

incorporated the pressure effects by further expanding each of the 2720 coefficients a_i, b_i, c_i, and d_i into binomials of the form $a_i = a_{i0} + a_{i1} \cdot f_P$, etc., where $f_P = \sqrt{P_{dyn}/P_0} - 1$ and $P_0 = 2$ nPa. That resulted in doubling the amount of unknown model coefficients, so that their final number (equal to the number of equations to be solved by the least squares algorithm) rose to 5440. Owing to the use of the singular value decomposition method [*Press et al.*, 1992] and parallelization of the fitting code, the problem nevertheless turned out computationally feasible, as demonstrated in the next sections.

The magnetospheric driving via the interplanetary magnetic field (IMF)-related processes could in principle be built into the model by further including into its coefficients of terms containing various interplanetary coupling functions, e.g., vB_s or more complex ones. While many possible options can be envisioned on that way, in this study we restricted ourselves to the easiest approach, based on binning the data into a few groups with respect to sliding average values of the *SYM-H* index and its time derivative. These two parameters can be interpreted as proxies representing the state of the magnetosphere in the course of a typical disturbance. Having fitted the model to thus generated subsets, we obtained magnetic field and electric current configurations, corresponding to principal phases of a storm, as described below in more detail.

3. Data

In this study we employed data of five missions: Geotail, Polar, Cluster, Time History of Events and Macroscale Interactions during Substorms (THEMIS), and Van Allen Space Probes (Radiation Belt Storm Probes (RBSP)), obtained between 1995 and 2015. Main stages and particulars of the data processing were described at length in *Tsyganenko et al.* [2015], and the reader is referred to that work for details. We used 5 min magnetic field and ephemeris vector averages, obtained from the original high-resolution data, with magnetosheath and solar wind intervals removed. All the data were tagged with concurrent interplanetary parameters from the OMNI source (http://omniweb.gsfc.nasa.gov/form/omni_min.html), time shifted to the subsolar bow shock location [*King and Papitashvili*, 2005]. The magnetospheric data were limited radially within 12 R_E and transformed into the solar-magnetic (SM) coordinate system.

To derive the magnetic field and electric current patterns during different storm phases, we created four data subsamples corresponding to restricted intervals of the 6 h centered average *SYM-H* index, $\langle SYM\text{-}H \rangle$, and its time derivative $D\langle SYM\text{-}H \rangle / Dt$. These parameters were defined as the weighted arithmetic means

$$\langle SYM\text{-}H \rangle(t) = \frac{1}{73} \sum_{k=-36}^{36} \left[SYM\text{-}H(t_k) \cos \frac{\pi k}{144} \right] \quad (9)$$

Table 1. Data Subsets Corresponding to Four Typical Magnetospheric States Over the Course of a Storm[a]

State	N	$\langle SYM\text{-}H\rangle$ (nT)	$D\langle SYM\text{-}H\rangle/Dt$ (nT/h)	$\langle B\rangle$ (nT)	$Q/\langle B\rangle$ (%)
Prestorm quiet time (QT)	41,611	[−20.0, −5.0]	[−0.5, 0.5]	20.8	42
Storm deepening (SD)	37,031	[−100.0, −40.0]	[−5.0, −2.0]	56.9	34
Main phase peak (MP)	35,439	[−100.0, −50.0]	[−1.0, 1.0]	57.5	32
Recovery phase (RP)	40,187	[−40.0, −20.0]	[2.5, 3.5]	32.7	34

[a]The quantities in the columns are the number of records N, the lower and upper limits of $\langle SYM\text{-}H\rangle$ and $D\langle SYM\text{-}H\rangle/Dt$, the RMS external field $\langle B\rangle = \{\langle|\mathbf{B}|^2\rangle\}^{1/2}$, and the RMS deviation of the model field over the subset $Q = \{\langle|\mathbf{B}_{obs} - \mathbf{B}_{mod}|^2\rangle\}^{1/2}$ expressed as a percentage of $\langle B\rangle$.

$$\frac{D\langle SYM\text{-}H\rangle}{Dt}(t) = \frac{1}{73}\sum_{k=-36}^{36}\left[SYM\text{-}H(t_k)\sin\frac{\pi k}{72}\right] \tag{10}$$

where $t_k = t + k/12$ are consecutive time moments (in hours) evenly distributed over the 6 h long averaging interval $[t-3, t+3]$, roughly commensurate with the average decay time of the ring current.

The idea behind introducing the 6 h averages $\langle SYM\text{-}H\rangle$ and $D\langle SYM\text{-}H\rangle/Dt$ in the form (9) and (10) goes back to *Sitnov et al.* [2008] (equations (5) and (6)). Its essence is to define two parameters that would allow us to sort the data records from the large "grand" set into smaller subsets, corresponding to four phases of a disturbance. Thus, (1) small values of both $\langle SYM\text{-}H\rangle$ and $D\langle SYM\text{-}H\rangle/Dt$ would refer to quiet time conditions (abbreviated henceforth as QT), (2) large negative $D\langle SYM\text{-}H\rangle/Dt$ indicate the storm deepening (SD) with rapidly growing near-Earth field depression, (3) large negative $\langle SYM\text{-}H\rangle$ but small $D\langle SYM\text{-}H\rangle/Dt$ correspond to conditions around the main phase peak (MP), and (4) positive $D\langle SYM\text{-}H\rangle/Dt$ against the background of moderately low $\langle SYM\text{-}H\rangle$ would manifest the recovery phase (RP). Specific intervals of $\langle SYM\text{-}H\rangle$ and $D\langle SYM\text{-}H\rangle/Dt$, the numbers of records in the subsets N, and the obtained statistical fit parameters $\langle B\rangle$ and $Q/\langle B\rangle$ are listed in Table 1, where $\langle B\rangle = \{\langle|\mathbf{B}|^2\rangle\}^{1/2}$ is the RMS external field and $Q = \{\langle|\mathbf{B}_{obs} - \mathbf{B}_{mod}|^2\rangle\}^{1/2}$ is the RMS deviation of the model field from data.

The role of the sine and cosine masks in (9) and (10) is to reduce the effects of shorter time scale fluctuations due to substorms, as discussed by *Sitnov et al.* [2008]. Note that unlike in the latter cited work and more recent papers by that team [*Sitnov et al.*, 2010; *Stephens et al.*, 2013, 2015], the foremost goal of the present study is to only test the ability of the new method to reproduce 3-D magnetospheric configurations at characteristic phases of a typical disturbance, rather than to describe their temporal evolution in the course of specific events.

Figure 2 illustrates the adopted selection of the data into subsets in the form of a color diagram, visualizing the distribution of data records in our grand set in the 2-D space of the state control parameters $\langle SYM\text{-}H\rangle$ and $D\langle SYM\text{-}H\rangle/Dt$. The color-coded quantity is the logarithm of the number of data records falling into 0.4 nT/h × 1.5 nT bins of the above parameters. One can see that most part of the data is concentrated within the yellow/red area $-50 \le \langle SYM\text{-}H\rangle \le 0$ and $-5 \le D\langle SYM\text{-}H\rangle/Dt \le 5$. The blue rectangles delineate the areas corresponding to four data subsets, representing different magnetospheric states/conditions as specified in Table 1.

Because of the very large difference of the data density between quiet and storm time conditions, and in view of the requirement for the subsets to contain nearly the same amount of data records, on the order of ~40,000, we chose relatively narrow parameter limits for the QT subset and applied a data thinning procedure. (The essence of the thinning method was to select only data records separated by time intervals no shorter than $\Delta t = 2$ h, if corresponding to the same spacecraft.) By contrast, to ensure enough data in the storm time SD, MP, and RP subsets, we had to use wider limits of the binning parameters, and no thinning was applied in those cases.

Figure 3 illustrates the spatial distribution of data in the MP subset, corresponding to the minimum of $\langle SYM\text{-}H\rangle$ (third column in Table 1). Distributions in Figure 3 (left and right) correspond to the equatorial and meridional projections in the SM coordinates, and the quantity shown by the color coding is the logarithm of the total

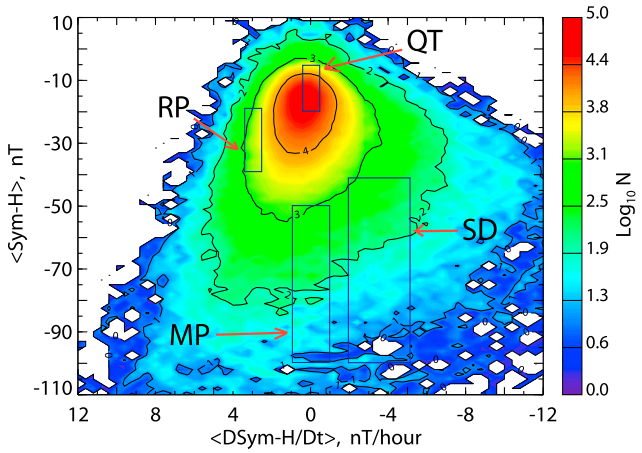

Figure 2. Distribution of the grand set data density in the 2-D space of parameters ⟨*SYM-H*⟩ and D⟨*SYM-H*⟩/D*t*. The blue rectangles delineate the areas, corresponding to four data subsets for different magnetospheric states/conditions, as specified in Table 1: (1) quiet time before storms (QT), (2) storm development phase (SD), (3) main phase peak (MP), and (4) recovery phase (RP). The color coding corresponds to the logarithm of the number of data records falling into 0.4 nT/h × 1.5 nT bins of the above parameters.

number *N* of data points contained inside the columns oriented parallel to *Z* and *Y* axes, respectively, with $0.5 \times 0.5 R_E$ cross-section area.

As one can see from the plots, the radial coverage is rather nonuniform, with numerous data gaps at $r \sim 7-12\,R_E$. The near-equatorial region $r \leq 5\,R_E$ on the nightside is best covered (as indicated by red/orange color), while on the dayside and in the high-latitude areas the data are much sparser. The spatial nonuniformity of the data is mostly due to the fact that the MP subset illustrated in Figure 3 corresponds to relatively rare storm events. Most of the data records in that sample are clustered into isolated sequences, corresponding to individual satellite orbits, which explains the ragged coverage pattern. By contrast, the QT subset (first column in Table 1; no plot shown) initially included many more records and was thinned before being used to fit the model. As a result, the data coverage in that case is much more regular and smooth.

4. Testing the Method

Before fitting the RBF model to actual spacecraft data, its performance was tested on an artificial "data" set, generated by using our recent empirical model [*Tsyganenko and Andreeva*, 2015, referred henceforth as TA15].

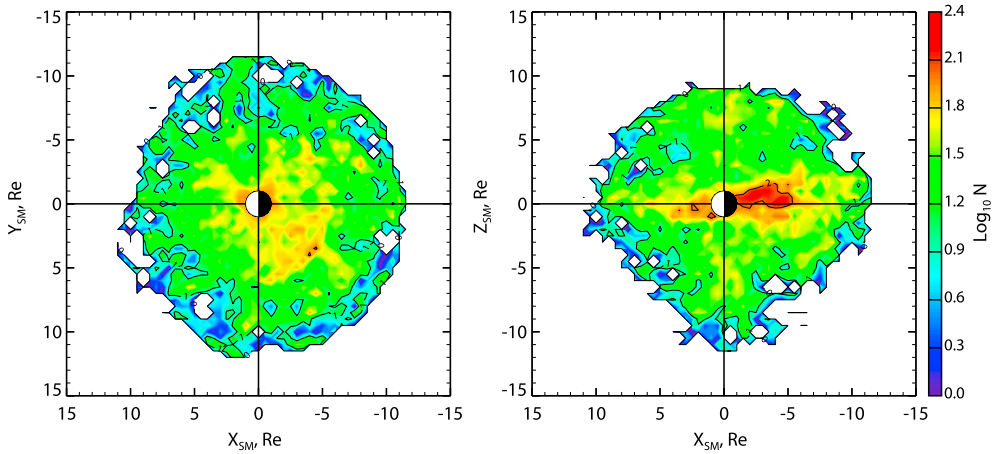

Figure 3. Illustrating the spatial coverage of the modeling region with data in the subset, corresponding to the main phase peak (MP). The panels display the integrated density of data points in projections onto (left) equatorial and (right) meridional planes.

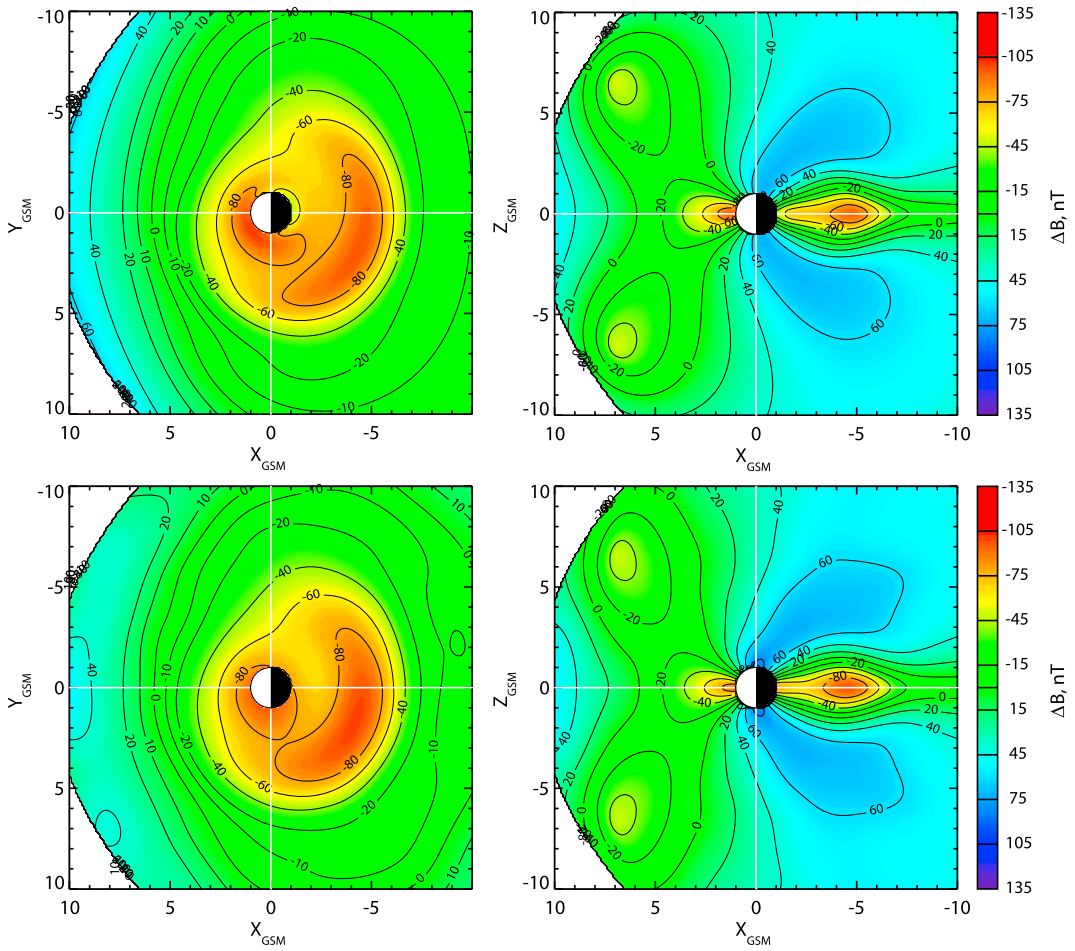

Figure 4. Comparing (top row) the TA15 target field with (bottom row) the reconstructed RBF model field. (left column) Equatorial distributions of $\Delta B = |\mathbf{B}_{\text{total}}| - |\mathbf{B}_{\text{dipole}}|$; (right column) meridional distributions of $\Delta B = |\mathbf{B}_{\text{total}}| - |\mathbf{B}_{\text{dipole}}|$. The plots correspond to a disturbed TA15 field with $N = 1.5$ and $P_{\text{dyn}} = 3.3$ nPa.

The goal was to assess the fidelity of the field reconstruction and to expose possible artifacts of the method, if any. The choice of the TA15 model as the reference data generator was motivated by its flexibility in describing a variety of realistic field configurations in the near magnetosphere at different interplanetary conditions.

Two different tests have been carried out on the basis of two subsamples, each containing ~35,000 data points, roughly matching the typical size of real data subsamples used in the fitting the RBF model to actual spacecraft observations. In order to generate well-pronounced dawn-dusk asymmetric field structures, the TA15 model parameters were set at values corresponding to highly disturbed conditions, with the driving N index equal to 1.5, IMF $B_y = -3$ nT, and IMF $B_z = -5$ nT.

The principal distinction between the two tests was in the distribution of the artificial data points in space. In the first experiment we distributed the data in a more regular manner, by randomly placing five points within a distance of 1 R_E around each of the $680 \times 2 = 1360$ RBF centers $\mathbf{R_i}$ in both northern hemispace and southern hemispace. Then the subsample was further expanded fivefold by having randomly assigned five different values of the dipole tilt angle ψ to each data point, within the range $|\psi| \leq 30°$. Since the solar wind pressure P_{dyn} entered in the RBF model coefficients as an independent parameter, its values for each data record were randomly scattered with the amplitude 0.5 nPa around the average value $P_{\text{dyn}} = 2.5$ nPa, in order to avoid ill conditioning of the matrix of linear equation system. Fitting the RBF model to thus generated set revealed a fairly close match between the reconstructed magnetic field and the target TA15 distribution. Specifically, the ratio $Q/\langle B \rangle$ of the RMS residual to the RMS TA15 field over the data set was found equal to ~0.17. This value might appear unexpectedly large, given the regularity and noiseless nature of the target field, as well as the relatively dense coverage of the modeling region by the RBF nodes. A closer inspection

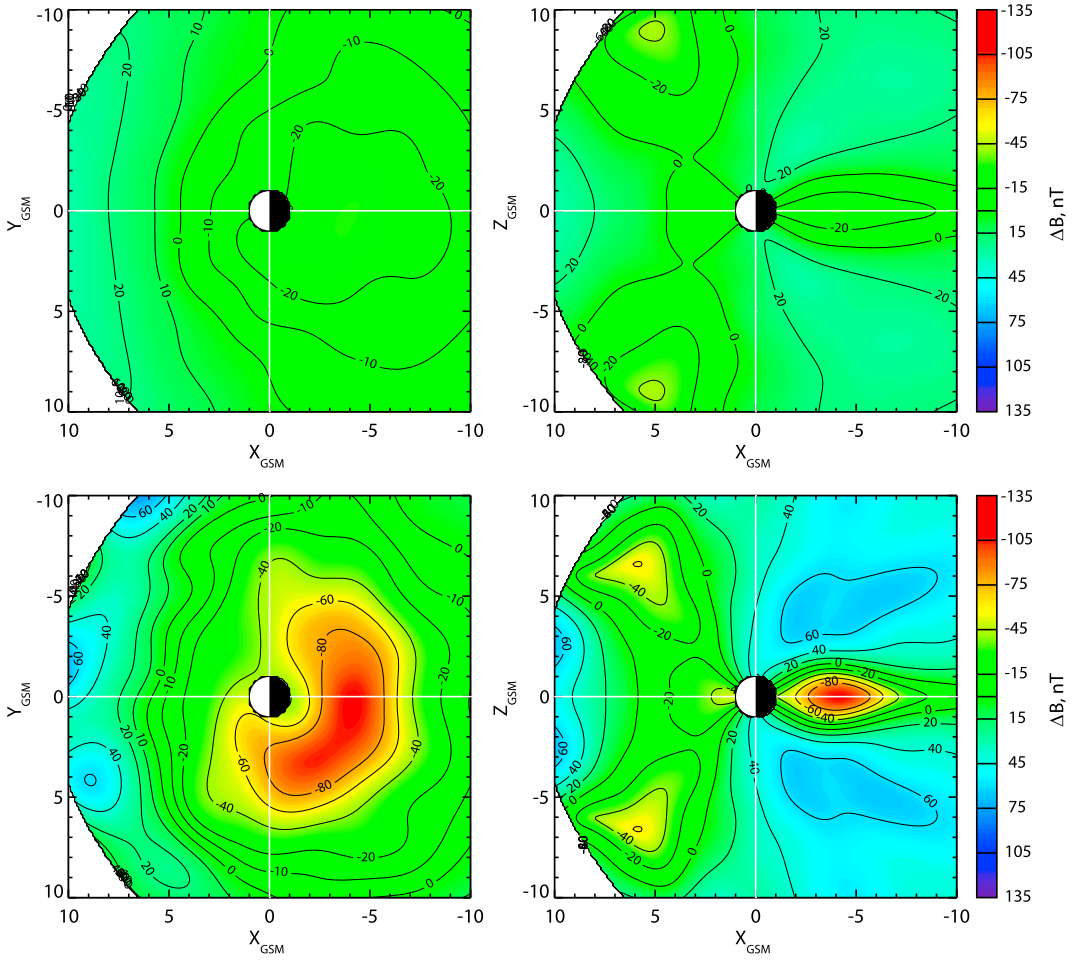

Figure 5. (left column) Equatorial and (right column) meridional distributions of the RBF model ΔB, derived from the data subsets, corresponding to (top row) quiet times (QT) and the (bottom row) storm deepening phase (SD). See Table 1 for the exact definition of magnetospheric conditions in terms of the *SYM-H* index and its time derivative.

showed that most of the discrepancy came from the high-latitude/low-altitude region, characterized by a relatively large contribution from the field-aligned currents. In that region, the spatial resolution of the RBF model is insufficient to reproduce the highly structured field of FACs, while the field magnitude is by at least a factor of 3–5 larger than in the equatorial magnetosphere.

The above conjecture was confirmed by the second test, whose goal was to assess the effect of spatial nonuniformity of the data on the field reconstruction accuracy. For this purpose, the target data were created by evaluating the reference model field at irregular set of points, corresponding to the actual locations of spacecraft observations, by contrast to the regular mesh of points used in the first experiment. More specifically, as an input for the TA15 reference model, we used the spacecraft SM locations $\{X, Y, Z\}$, dipole tilt angles ψ, and the solar wind pressures P_{dyn}, corresponding to real data records from the SD subsample for the initial part of the storm main phase. In that fitting run, the relative RMS deviation was found as low as $Q/\langle B\rangle = 0.06$, i.e., roughly only a third of that obtained in the first experiment. Such a dramatic improvement is due to the fact that the spatial density of the real data rapidly decreases toward Earth, with only a relatively small number of Van Allen data records in the distance interval $2 \le r \le 3\,R_E$. The share of the FAC contribution to the residual field is therefore much smaller, which explains much better fitting accuracy in the second case.

Figure 4 compares equatorial (left column) and meridional (right column) distributions of the TA15 target field (top row) and the reconstructed RBF model field (bottom row), based on the spatially nonuniform set of data points employed in the second test. The displayed quantity in both plots is the difference $\Delta B = |\mathbf{B}_{total}| - |\mathbf{B}_{dipole}|$ between the scalar magnitudes of the total and purely dipolar magnetic field (the so-called "scalar

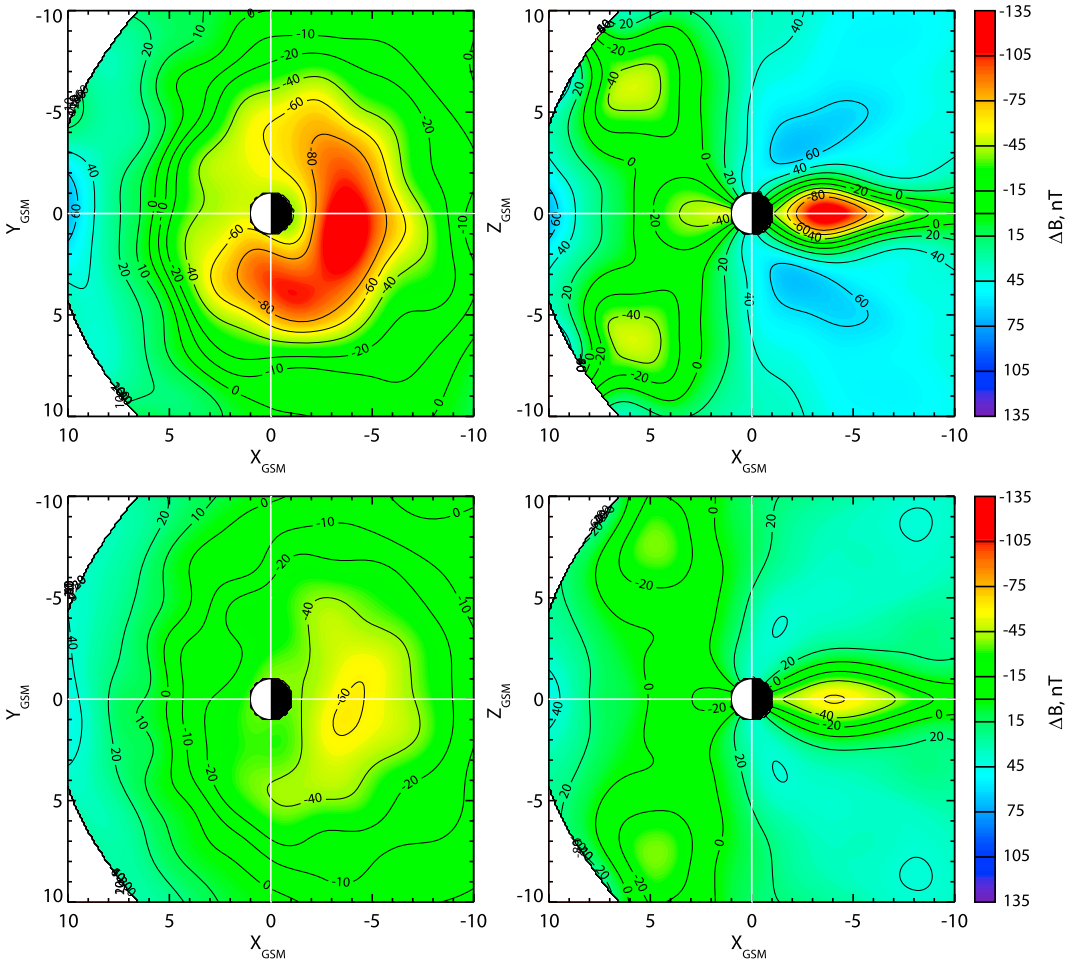

Figure 6. Same as in Figure 5 but for the (top row) main phase peak (MP) centered around the time of $D\langle SYM\text{-}H\rangle/Dt = 0$ and for the (bottom row) recovery phase (RP).

anomaly," first introduced by *Sugiura et al.* [1971]). Red/yellow colors correspond to the areas of depressed field inside the ring current and in the dayside cusps, while blue/magenta colors indicate the compressed field regions near the subsolar magnetopause and in the tail lobes. One can see a close agreement between the target and reconstructed fields not only in terms of the general pattern with a strong dawn-dusk asymmetry but also in the location and shape of individual equal ΔB contours.

5. Fitting to Real Data: Results

Having thus verified the feasibility of the modeling method, we recovered magnetic field configurations from the real data subsets, representing four characteristic storm phases listed in Table 1. The values of the ratio $Q/\langle B\rangle$ expressed as percentages were found to vary in the range between ~32% and ~42%, which is at the lower end of the typical range (between ~40% and ~60%) obtained in previous empirical models. Our main results are graphically presented in Figures 5 and 6. Both figures show in their left and right columns, respectively, the equatorial and meridional distributions of ΔB for zero dipole tilt. Note that the RBF model is based only on data inside the magnetosphere and, by its very construction, does not explicitly include a magnetopause. The boundary shown in the figures is plotted only for the reader's orientation and corresponds to an average position of the magnetopause according to the model by *Lin et al.* [2010]. Figure 5 shows the model ΔB distributions corresponding to the QT (top row) and SD (bottom row) subsets. Figure 6 displays in a similar format two distributions, corresponding to the MP (top row) and RP (bottom row) subsets. As can be seen from the plots, the reconstructed field reveals all principal features of the magnetospheric structure and their basic changes associated with the principal stages of a disturbance. The QT configuration is characterized by

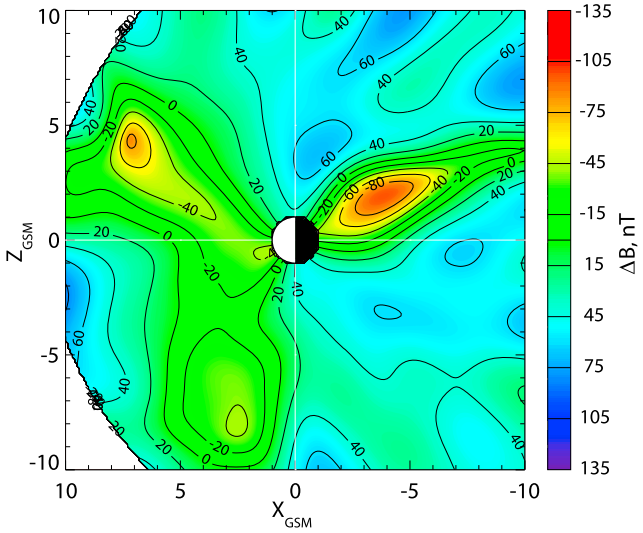

Figure 7. Same as in Figure 5 but for the tilted magnetospheric configuration with the dipole tilt $\psi = 30°$. The diagram corresponds to the SD variant of the model.

generally weak external field without any significant dawn-dusk asymmetry. In a sharp contrast, the most outstanding feature of the storm main phase is a dramatically asymmetric ΔB, especially in the MP case, when the inner field depression not only tightly envelops Earth in the midnight/premidnight sector but also spreads well on the dayside, with the ΔB lowest values reaching −135 nT at geocentric distances $3 \leq r \leq 4\,R_E$. At the ground level, the model ΔB varies between −50 and −60 nT, in good agreement with the average $\langle SYM\text{-}H \rangle \approx -61$ nT, calculated for the corresponding data subset with the actual *SYM-H* values between −100 and −50 nT (Table 1). In the RP case the magnetic field exhibits a much more symmetric configuration. Note also a distinct deepening of the polar cusp depression due to the diamagnetism of injected magnetosheath plasma [*Tsyganenko and Russell*, 1999; *Tsyganenko*, 2009], clearly seen in the meridional projections and especially pronounced in the SD case (Figure 5, bottom right). The somewhat "wavy" shape of ΔB contours and the local positive peaks of the compressed field near the subsolar magnetopause in Figure 5 is unlikely to be a real feature; they rather result from nonuniformity of the data, combined with the discrete structure of the RBF meshwork.

Figure 7 displays a meridional diagram of ΔB for the SD variant in the same format as in Figures 5 and 6 but for a tilted configuration with the dipole tilt angle $\psi = 30°$. A feature that immediately hits the eye is a dramatic asymmetry between the southern and northern cusps. First, the corresponding diamagnetic depression magnitudes are largely different: in the northern cusp, exposed head-on to the solar wind, the peak depression reaches −80 nT, while in the leeward southern cusp it is nearly twice weaker. The second interesting detail is that the northern depression penetrates deeply toward low altitudes in the shape of a sharp tongue, while the southern depression is much more rounded and less structured. On the nightside one clearly sees the well-known hinging of the current with its gradual deflection from the SM equator in the direction of the solar wind.

6. Discussion

The first question, which naturally arises as soon as one derives from data a magnetic field model, is what the underlying distribution of the electric current $\mathbf{j} = \nabla \times \mathbf{B}/\mu_0$ looks like. Note that the amount of new knowledge gained in such a way from data is inevitably reduced when using models based on a limited number of simple modules with a few free parameters. For example, it is in principle impossible to empirically discern from data a bifurcated structure of a current sheet on the basis of a standard Harris-type single-sheet model. On the contrary, lifting empirical a priori assumptions enhances the model's flexibility and makes it possible to extract more and more information from the data.

In the previous sections we introduced the basics of the RBF model and described first results of implementing it to derive from data actual magnetospheric configurations. The proposed method lends maximum flexibility

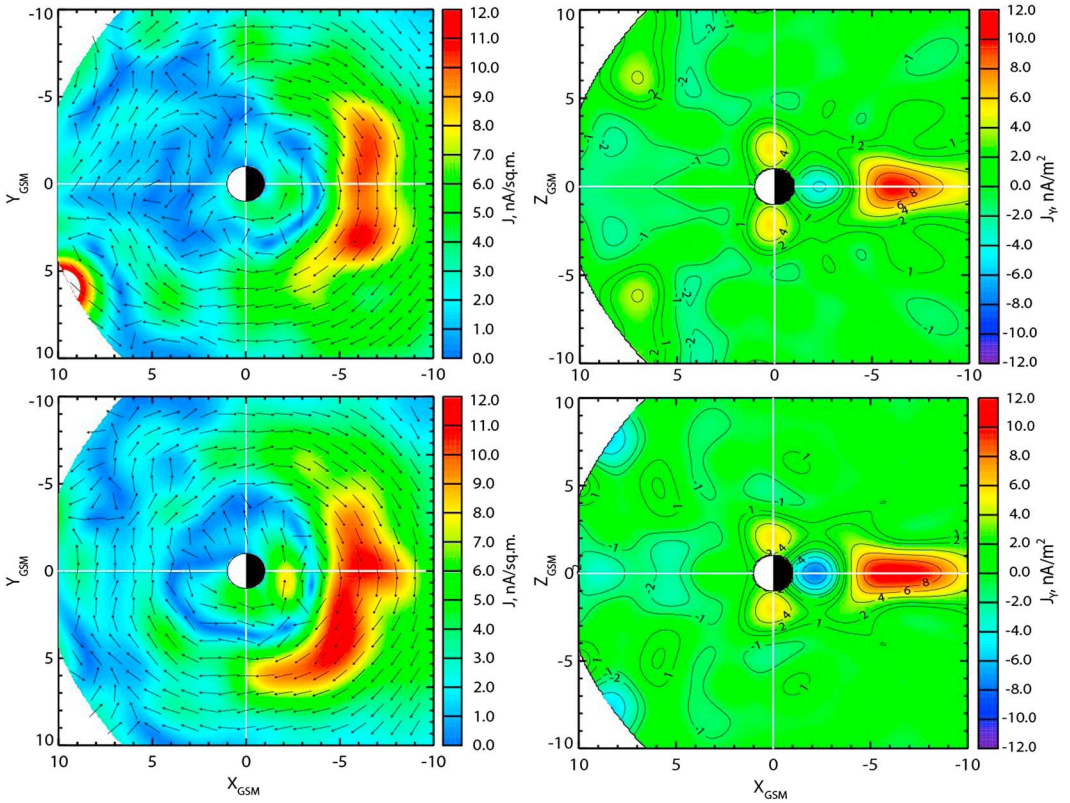

Figure 8. (left column) Equatorial and (right column) meridional distributions of the electric current volume density for the (top row) SD during the falloff of *SYM-H* index and for the (bottom row) MP conditions. The color coding in the panels corresponds, respectively, to the total current $|\mathbf{j}|$ (Figure 8, left column) and its dawn-dusk component j_y (Figure 8, right column). Arrows in Figure 8 (left column) indicate the direction of the **j** vectors.

to the model, by contrast to the standard approach, based on a few modules with built-in a priori assumptions about the external sources. Therefore, we felt it very intriguing to examine the electric current distribution in the new model. An important caveat should be mentioned before we proceed to results: the fitting algorithm deals with the magnetic field, rather than with the electric current, and yields a fairly smooth model distribution of the **B** vector. Taking its curl, however, greatly magnifies the effect of small spatial irregularities of **B**, which inevitably results in a much bumpier distribution of $\mathbf{j} = \nabla \times \mathbf{B}/\mu_0$. One should therefore take caution when interpreting the obtained **j** patterns, since it is often difficult to tell real features from artifacts.

Figure 8 (top row) shows equatorial and meridional distributions of the numerically calculated electric current volume density according to the RBF model, based on storm time data in the SD subset with negative $D\langle SYM\text{-}H\rangle/Dt$ (second column in Table 1). Figure 8 (bottom row) illustrates the MP case with $D\langle SYM\text{-}H\rangle/Dt \sim 0$ (third column in Table 1). The colors in the equatorial (Figure 8, left column) and meridional (Figure 8, right column) distributions represent, respectively, the absolute magnitude of the current density $|\mathbf{j}|$ and its j_y component (note different limits in the corresponding color bars). The arrows in the equatorial diagrams show the direction of the **j** vector. In the meridional projections, yellow/red colors correspond to positive polarity of j_y (westward current), and light/dark blue colors indicate negative (eastward) j_y.

The first thing to note is that all principal magnetospheric current systems are clearly revealed in the diagrams, despite the complete absence in the RBF model of any preconceived assumptions on the field source geometry. On the nightside, the current flows mainly in the azimuthal westward direction, with a significantly enhanced density in the midnight/premidnight sector at distances $5 \le r \le 8\,R_E$. In the meridional diagrams that region reveals itself as the ring current, smoothly merging with the inner part of tail current sheet, about 2–3 R_E thick. Quite remarkably, in both meridional diagrams one can even see a bifurcation of the current at its inner edge, with a formation of a pair of "horns," protruding earthward in the shape of a fork-like structure. Such structures arise due to the mapping of the equatorial plasma pressure (and its transverse gradient) along

the quasi-dipolar field lines; they were revealed in theoretical models as early as in 1960s [*Sozou and Windle*, 1969, Figure 1] and are routinely reproduced in MHD simulations [e.g., *Kuznetsova et al.*, 2007, Figure 5] as well as in the empirical modeling of 3-D force-balanced plasma and magnetic field structures [*Yue et al.*, 2013, 2015]. The fact that the horns show up in both cases, based on completely different data subsets, provides a convincing evidence in support of their real nature and, at the same time, confirms the ability of the method to resolve even fine details of the actual magnetospheric currents.

An outstanding feature in both equatorial plots (Figure 8, left column) is the strong dawn-dusk asymmetry of the currents, especially pronounced in Figure 8 (left column, bottom row), corresponding to the MP variant of the model. A similar "tusk-like" pattern was obtained earlier in the TS07 model [*Tsyganenko and Sitnov*, 2007, Figure 8a; *Sitnov et al.*, 2008, Figure 4c], where a significant part of the currents extended much farther out and reached the postnoon magnetopause. In our model, however, both the electric current and the associated ΔB depression are found to concentrate at closer radial distances and envelop Earth in the azimuthal direction, without any significant current flowing toward the duskside magnetopause.

Comparing the plots for the storm development (SD) phase (Figure 8, top row) with those for the storm peak (MP) conditions reveals first of all a general intensification of the nightside currents. One also clearly sees that the inner edge of the westward current shifts closer to Earth at the storm peak.

On the dayside the currents are significantly weaker than on the nightside, but the general flow direction remains mostly westward. A separate feature worth to mention is the eastward current at $r \sim 2-3\,R_E$, associated with the reversed (outward) gradient of the particle pressure $P(r)$ in the innermost magnetosphere and required to maintain force balance between plasma and magnetic stresses. Its existence was theoretically predicted still at the dawn of the space era [e.g., *Akasofu and Chapman*, 1961] and confirmed by a direct statistical analysis of magnetometer data [*Le et al.*, 2004]. The eastward component of the ring current was taken into account in the T02 and TS05 empirical models [*Tsyganenko*, 2000, 2002a, 2002b; *Tsyganenko and Sitnov*, 2005], though its effect on the field line configuration is essentially negligible due to much stronger main geomagnetic field in that region. As can be seen in Figure 8, the storm time eastward current is significantly asymmetric, with much higher current densities in the premidnight sector; this finding agrees with the result of *Le et al.* [2004, Figure 7], as well as with that by *Stephens et al.* [2015, Figure 7].

Scattered areas with a weak and irregular eastward current can also be seen in the outermost region near the dayside magnetopause. Two possible causes can be suggested here, the first one being a purely computational fringe effect of the RBF meshwork boundary at $R = 12\,R_E$, combined with fast decrease of the data spatial density beyond that distance. The second cause can be a real effect of the Chapman-Ferraro boundary currents: even though the extramagnetospheric data were filtered out, some portion of them could evade detection, slip into the modeling subsets, and result in substantial jumps of **B** vector, correctly interpreted by the RBF model as due to the magnetopause current. This conjecture gains support from the fact that the eastward boundary currents were not found in the diagrams corresponding to the QT and RP subsets (not shown). In those cases, the average solar wind pressure was lower and the magnetopause expanded outward beyond the boundary of the modeling region.

In the meridional projections (Figure 8, right column), a strong day-night asymmetry of both the outer (westward) and inner (eastward) currents is also clearly seen. On the dayside the ring current is weaker and much more spread out in the north-south direction. Also, in Figure 8 (top row), corresponding to the SD phase, the distant ring current bifurcates on the dayside into a pair of local peaks of j_y within a short distance from the magnetopause. This can be interpreted as a manifestation of particle trapping onto the so-called Shabansky orbits in the localized minimum B regions [*Antonova and Shabansky*, 1968; *McCollough et al.*, 2012], which in turn may result in branching of the distant dayside ring current [*Antonova et al.*, 2013]. In Figure 8 (bottom row), corresponding to the MP subset, the bifurcated currents shift to even higher latitudes (light blue spots near the boundary), which may be due to poleward excursion of the cusps following the change of IMF B_z polarity at the end of the main phase.

Another feature apparent in both meridional panels on the dayside is a pair of elongated yellow/bluish spots, located at middle/high latitudes at $r \sim 7-10\,R_E$. These are the diamagnetic currents, enveloping the polar cusps and associated with the penetrated magnetosheath plasma, which results in broad magnetic field depressions, clearly seen in Figures 5 (right column) and 6 (right column) and in Figure 7, mentioned in the previous section. Their polarity ($j_y<0$ poleward and $j_y>0$ equatorward from the cusps) corresponds to a

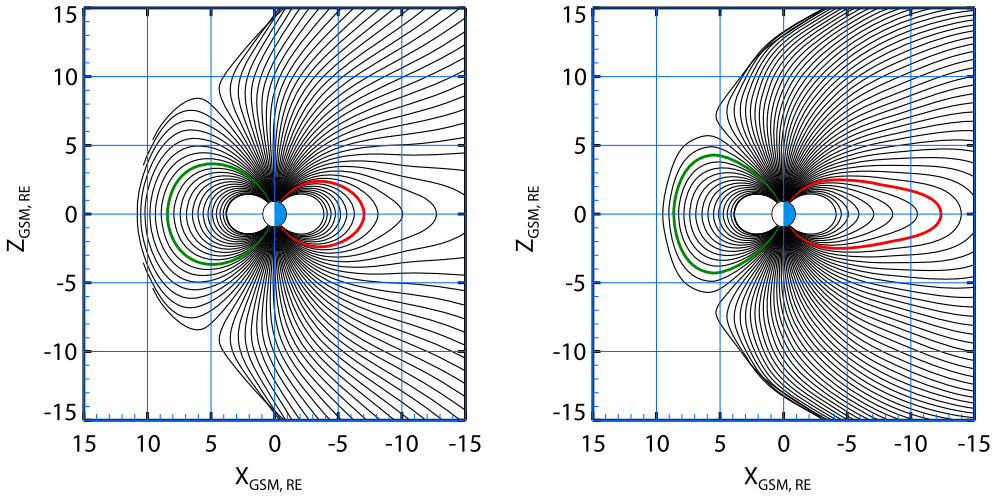

Figure 9. Meridional field line configurations, corresponding to the (left) QT and (right) SD phases. Field lines with noon foot point at 71° and midnight foot point at 66° of SM latitude are shown by green and red, respectively.

disturbance field, directed oppositely to the local total **B**, thus resulting in weaker field magnitude inside the cusp "funnels". According to the model, during the SD phase (Figure 8, top row), usually associated with large southward IMF, the cusp currents are significantly stronger than at the peak of a storm, often accompanied by an abrupt northward IMF reversal (MP, Figure 8 (bottom row)).

A conspicuous detail in both panels is a pair of bright yellow spots immediately above the northern and southern polar caps, indicating a strong dawn-dusk current with the peak value $j_y \sim 5$ nA/m^3 at $r \sim 2\,R_E$. This is nothing more than the net closure current of the Regions 1 and 2 field-aligned currents combined, spread out across unrealistically large area because of insufficient spatial resolution of the RBF meshwork above the ionosphere and lack of data at $r \leq 2\,R_E$. In actuality, the Birkeland currents converge toward Earth, so that at low altitudes their transverse scale shrinks to a few tenths of R_E or less, which is well below the RBF grid resolution adopted in this study. A more accurate modeling of such structures at higher resolution can be done simply by shrinking/reconfiguring the entire grid (thus increasing the node density) and shifting/focusing it on a specific region of interest, like a magnifying glass. This is a separate interesting research area, which we relegate for later studies.

To quantitatively visualize the modeling results in terms of the reconstructed field line configuration, two plots were generated, corresponding to the QT period and for the SD phase, presented in two panels of Figure 9. To help the readers estimate the extent of the field line stretch on the nightside and of the magnetic flux erosion on the dayside, the lines with foot point SM latitudes 66° on the nightside and 71° on the dayside were highlighted with red and green colors, respectively. In the QT case (Figure 9, left), the cusp field lines map as high as ~80°, while the midnight field line with foot point at 66° remains deep in the inner magnetosphere and maps as close as $X = -6\,R_E$. By contrast, in the SD case (Figure 9, right) the cusps shift equatorward to ~73° and the 66° foot point line stretches much farther out and crosses the equatorial plane at $X = -12\,R_E$.

In conclusion, we note that the grid resolution and a good data coverage are necessary but not sufficient conditions to accurately reconstruct the actual magnetic field configurations. Using archived spacecraft data inevitably poses a problem of optimal selection of data into subsets, best reflecting a specific state of the magnetosphere. In the present work we limited ourselves to a rather simple method, in which the magnetospheric states were classified into four cases, based on the averaged *SYM-H* index and its time derivative. Future studies should place more emphasis on that subject, with the ultimate goal to find an optimal way to take into account prehistory of the solar wind and IMF conditions. A more distant but no less attractive future application of the RBF approach can be envisioned: reconstructing instantaneous magnetospheric configurations on the basis of a multisatellite large-scale constellation of the magnetosphere monitors (e.g., *Tsyganenko* [1998], and other articles in that volume).

7. Summary

To summarize, we developed a new method to reconstruct from data the magnetospheric magnetic field by expanding its toroidal and poloidal parts into sums of radial basis functions over a regular 3-D grid covering the modeling region. The method allows one to obtain the magnetic field without any a priori assumptions on the geometry of its sources. Provided there is a sufficient amount of spacecraft data covering the region of interest, a RBF model with a remarkably high spatial resolution can be created. Even in the presented version covering the magnetosphere in the range $r \leq 12\,R_E$ with a resolution on the order of $\sim 0.5 - 1.0\,R_E$, we were able to reproduce such fine details as the diamagnetic currents in the cusps, the fork-like bifurcation of the inner edge of the current sheet, and the asymmetric westward and eastward ring currents. On the other hand, lack of data and insufficient grid resolution at low altitudes resulted in only a blurred image of the field-aligned currents above the polar caps. The proposed method can be used as a tool to study the magnetospheric currents in selected areas by focusing the RBF grid on a local region of interest.

Acknowledgments

The data used to derive the above described results are available on request from the authors. It is a pleasure to acknowledge the teams and PIs of all experiments whose data contributed to this study. Geotail MGF data were provided by the PIs, S. Kokubun (STEL) and T. Nagai (Tokyo Institute of Technology, Japan). The data of Polar MGF experiment were made available online by the UCLA team led by the PI C. T. Russell. The Cluster magnetometer, spacecraft ephemeris, and CIS instrument data were obtained from the NSSDC CDAWEB online facility (originally provided by the following PIs: A. Balogh, M. Tatrallyay, and H. Reme, respectively). NASA contract NAS5-02099 and V. Angelopoulos are acknowledged for use of THEMIS mission data; specifically, K. H. Glassmeier, U. Auster, and W. Baumjohann are acknowledged for the use of FGM data provided under the lead of the Technical University of Braunschweig and with financial support through the German Ministry for Economy and Technology and the German Center for Aviation and Space (DLR) under contract 50 OC 0302. We acknowledge the NASA Van Allen Probes and Craig Kletzing (University of Iowa) for use of the RBSP-A and RBSP-B EMFISIS data. High-Resolution OMNI interplanetary data were obtained from the SPDF OMNIWEB interface (R. McGuire, N. Papitashvili). This work was supported by the Russian Science Foundation grant 14-17-00072.

References

Akasofu, S.-I., and S. Chapman (1961), The magnetic field of a model radiation belt, numerically computed, *J. Geophys. Res.*, *66*, 4013–4026.

Antonova, A. E., and V. P. Shabansky (1968), Structure of the geomagnetic field at great distance from the Earth, *Geomagn. Aeron.*, *8*, 801–811.

Antonova, E. E., I. P. Kirpichev, V. V. Vovchenko, M. V. Stepanova, M. O. Riazantseva, M. S. Pulinets, I. L. Ovchinnikov, and S. S. Znatkova (2013), Characteristics of plasma ring, surrounding the Earth at geocentric distances ~7–10 R_E, and magnetospheric current systems, *J. Atm. Sol. Terr. Phys.*, *99*, 85–91.

Buhmann, M. (2003), *Radial Basis Functions: Theory and Implementations*, Cambridge Univ. Press, Cambridge, U. K.

Gershenfeld, N. (2003), *The Nature of Mathematical Modeling*, Cambridge Univ. Press, Cambridge, U. K.

King, J. H., and N. E. Papitashvili (2005), Solar wind spatial scales and comparisons of hourly Wind and ACE plasma and magnetic field data, *J. Geophys. Res.*, *110*, A02104, doi:10.1029/2004JA010649.

Kosik, J. C. (1989), Quantitative magnetic field model including magnetospheric ring current, *J. Geophys. Res.*, *94*, 12,020–12,026.

Kosik, J. C. (1998), A quantitative model of the magnetosphere with poloidal vector fields, *Ann. Geophys.*, *16*, 1557–1566.

Kurihara, Y. (1965), Numerical integration of the primitive equations on a spherical grid, *Mon. Weather Rev.*, *93*(7), 399–415.

Kuznetsova, M. M., M. Hesse, L. Rastaetter, A. Taktakishvili, G. Toth, D. L. De Zeeuw, A. Ridley, and T. I. Gombosi (2007), Multiscale modeling of magnetospheric reconnection, *J. Geophys. Res.*, *112*, A10210, doi:10.1029/2007JA012316.

Le, G., C. T. Russell, and K. Takahashi (2004), Morphology of the ring current derived from magnetic field observations, *Ann. Geophys.*, *22*, 1267–1295, doi:10.5194/angeo-22-1267-2004.

Lin, R. L., X. X. Zhang, S. Q. Liu, Y. L. Wang, and J. C. Gong (2010), A three-dimensional asymmetric magnetopause model, *J. Geophys. Res. Space Physics*, *115*, A04207, doi:10.1029/2009JA014235.

McCollough, J. P., S. R. Elkington, and D. N. Baker (2012), The role of Shabansky orbits in compression-related electromagnetic ion cyclotron wave growth, *J. Geophys. Res.*, *117*, A01208, doi:10.1029/2011JA016948.

Mead, G. D., and D. H. Fairfield (1975), A quantitative magnetospheric model derived from spacecraft magnetometer data, *J. Geophys. Res.*, *80*, 523–534.

Press, W. H., S. A. Teukolsky, W. T. Vetterling, and B. P. Flannery (1992), *Numerical Recipes*, 2nd ed., Cambridge Univ. Press, New York.

Sitnov, M. I., N. A. Tsyganenko, A. Y. Ukhorskiy, and P. C. Brandt (2008), Dynamical data-based modeling of the stormtime geomagnetic field with enhanced spatial resolution, *J. Geophys. Res.*, *113*, A07218, doi:10.1029/2007JA013003.

Sitnov, M. I., N. A. Tsyganenko, A. Y. Ukhorskiy, B. J. Anderson, H. Korth, A. T. Y. Lui, and P. C. Brandt (2010), Empirical modeling of a CIR-driven magnetic storm, *J. Geophys. Res.*, *115*, A07231, doi:10.1029/2009JA015169.

Sozou, C., and D. W. Windle (1969), Non-linear symmetric inflation of a magnetic dipole, *Planet. Space Sci.*, *17*, 999–1008.

Stephens, G. K., M. I. Sitnov, J. Kissinger, N. A. Tsyganenko, R. L. McPherron, H. Korth, and B. J. Anderson (2013), Empirical reconstruction of storm time steady magnetospheric convection events, *J. Geophys. Res. Space Physics*, *118*, 6434–6456, doi:10.1002/jgra.50592.

Stephens, G. K., M. I. Sitnov, A. Y. Ukhorskiy, E. C. Roelof, N. A. Tsyganenko, and G. Le (2015), Empirical modeling of the storm-time innermost magnetosphere using Van Allen Probes and THEMIS data: Eastward and banana currents, *J. Geophys. Res. Space Physics*, *120*, 157–170, doi:10.1002/2015JA021700.

Stern, D. P. (1976), Representation of magnetic fields in space, *Rev. Geophys.*, *14*, 199–214.

Sugiura, M., B. G. Ledley, T. L. Skillman, and J. P. Heppner (1971), Magnetospheric-field distortions observed by Ogo 3 and 5, *J. Geophys. Res.*, *76*, 7552–7565.

Tsyganenko, N. A. (1989), A magnetospheric magnetic field model with a warped tail current sheet, *Planet. Space Sci.*, *37*, 5–20.

Tsyganenko, N. A. (1998), Toward real-time magnetospheric mapping based on multi-probe space magnetometer data, in *Science Closure and Enabling Technologies for Constellation Class Missions*, edited by V. Angelopoulos and P. V. Panetta, pp. 84–90, UCLA, Berkeley, Calif.

Tsyganenko, N. A. (2000), Modeling the inner magnetosphere: The asymmetric ring current and Region 2 Birkeland currents revisited, *J. Geophys. Res.*, *105*, 27,739–27,754.

Tsyganenko, N. A. (2002a), A model of the near magnetosphere with a dawn-dusk asymmetry: 1. Mathematical structure, *J. Geophys. Res.*, *107*(A8), 1179, doi:10.1029/2001JA000219.

Tsyganenko, N. A. (2002b), A model of the near magnetosphere with a dawn-dusk asymmetry: 2. Parametrization and fitting to observations, *J. Geophys. Res.*, *107*(A8), 1176, doi:10.1029/2001JA000220.

Tsyganenko, N. A. (2009), Magnetic field and electric currents in the vicinity of polar cusps as inferred from Polar and Cluster data, *Ann. Geophys.*, *27*, 1573–1582, doi:10.5194/angeo-27-1573-2009.

Tsyganenko, N. A., and C. T. Russell (1999), Magnetic signatures of the distant polar cusps: Observations by Polar and quantitative modeling, *J. Geophys. Res.*, *104*, 24,939–24,955.

Tsyganenko, N. A., and M. I. Sitnov (2005), Modeling the dynamics of the inner magnetosphere during strong geomagnetic storms, *J. Geophys. Res.*, *110*, A03208, doi:10.1029/2004JA010798.

Tsyganenko, N. A., and M. I. Sitnov (2007), Magnetospheric configurations from a high-resolution data-based magnetic field model, *J. Geophys. Res.*, *112*, A06225, doi:10.1029/2007JA012260.

Tsyganenko, N. A., and V. A. Andreeva (2015), A forecasting model of the magnetosphere driven by an optimal solar wind coupling function, *J. Geophys. Res. Space Physics*, *120*, 8401–8425, doi:10.1002/2015JA021641.

Tsyganenko, N. A., V. A. Andreeva, and E. I. Gordeev (2015), Internally and externally induced deformations of the magnetospheric equatorial current as inferred from spacecraft data, *Ann. Geophys.*, *33*, 1–11, doi:10.5194/angeo-33-1-2015.

Wolf-Gladrow, D. A. (1987), *An Introduction to Poloidal and Toroidal Fields*, Mitteilungen aus dem Institut fuer Geophysik und Meteorologie der Universitaet zu Koeln, Germany.

Yue, C., C.-P. Wang, S. G. Zaharia, X. Xing, and L. Lyons (2013), Empirical modeling of plasma sheet pressure and three-dimensional force-balanced magnetospheric magnetic field structure: 2. Modeling, *J. Geophys. Res. Space Physics*, *118*, 6166–6175, doi:10.1002/2013JA018943.

Yue, C., C.-P. Wang, Y. Nishimura, K. R. Murphy, X. Xing, L. Lyons, M. Henderson, V. Angelopoulos, A. T. Y. Lui, and T. Nagai (2015), Empirical modeling of 3-D force-balanced plasma and magnetic field structures during substorm growth phase, *J. Geophys. Res. Space Physics*, *120*, 6496–6513, doi:10.1002/ 2015JA021226.